

OpenGraph: Open-Vocabulary Hierarchical 3D Graph Representation in Large-Scale Outdoor Environments

Yinan Deng, Jiahui Wang, Jingyu Zhao, Xinyu Tian, Guangyan Chen, Yi Yang, Yufeng Yue*

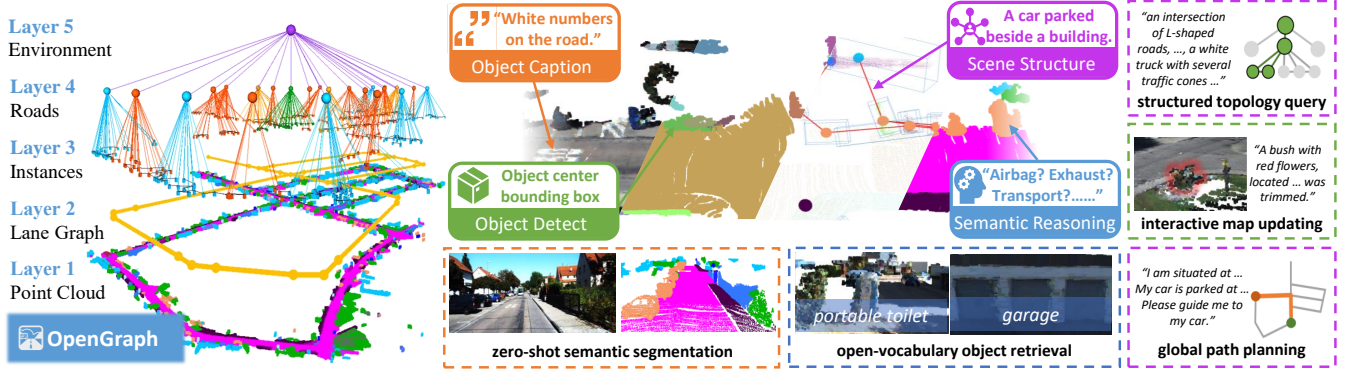


Fig. 1: We introduce **OpenGraph**, a framework for representing open-vocabulary hierarchical 3D graphs in large-scale outdoor environments. OpenGraph facilitates various downstream tasks, including zero-shot semantic segmentation, open-vocabulary object retrieval, structured topology query, global path planning, interactive map updating, and so on.

Abstract—Environment maps endowed with sophisticated semantics are pivotal for facilitating seamless interaction between robots and humans, enabling them to effectively carry out various tasks. Open-vocabulary maps, powered by Visual-Language models (VLMs), possess inherent advantages, including multimodal retrieval and open-set classes. However, existing open-vocabulary maps are constrained to closed indoor scenarios and VLM features, thereby diminishing their usability and inference capabilities. Moreover, the absence of topological relationships further complicates the accurate querying of specific instances. In this work, we propose OpenGraph, a representation of open-vocabulary hierarchical graph structure designed for large-scale outdoor environments. OpenGraph initially extracts instances and their captions from visual images using 2D foundation models, encoding the captions with features to enhance textual reasoning. Subsequently, 3D incremental panoramic mapping with feature embedding is achieved by projecting images onto LiDAR point clouds. Finally, the environment is segmented based on lane graph connectivity to construct a hierarchical graph. Validation results from real public dataset SemanticKITTI demonstrate that, even without fine-tuning the models, OpenGraph exhibits the ability to generalize to novel semantic classes and achieve the highest segmentation and query accuracy. The source code of OpenGraph is publicly available at <https://github.com/BIT-DYN/OpenGraph>.

I. INTRODUCTION

Accurate representation of 3D scenes is pivotal for robots to comprehend and reconstruct their environments, playing a vital role in various subsequent robotic tasks. Occupancy

This work is partly supported by the National Natural Science Foundation of China under Grant 62003039, 61973034, U193203, 62173042 the Changjiang Scholars Programme of China under Grant No. T2014224. (Corresponding Author: Yufeng Yue, yueyufeng@bit.edu.cn)

All authors are with School of Automation, Beijing Institute of Technology, Beijing, 100081, China.

maps [1] stand out as the most prevalent technique for building maps, allowing for the retrieval of geometric scene properties. By discerning obstacle positions and shapes, these maps facilitate spatial navigation for autonomous obstacle avoidance. With the advancement of deep learning technology, semantic information, which denotes object class, is incorporated into classic geometric maps [2]. This integration enables robots to achieve semantic-level intelligent navigation. However, such semantics are confined to predefined labels during the training phase, presenting challenges in heuristic comprehension and effective utilization.

In recent years, the widespread adoption of visual-language models (VLMs) [3]–[5] and large language models (LLMs) [6]–[8] has opened avenues for encapsulating high-level conceptual semantics in maps. These foundation models, trained on extensive web-based datasets, can uncover novel objects and derive simplistic understandings at inference time. Consequently, they enable cognitive navigation that mirrors human thought processes. However, existing open-vocabulary map building approaches are currently limited to structured indoor environments devoid of dynamic objects. Moreover, they crudely leverage VLM features for semantic map comprehension. These features are derived from VLMs encoding both images and text into a unified feature space through adversarial learning, but they lack sophisticated reasoning capabilities. Additionally, the absence of hierarchical topological relations introduces challenges for querying specific instances.

To overcome the aforementioned challenges, this paper proposes a novel framework for open-vocabulary hierarchical 3D graph representation, called OpenGraph. Unlike

approaches directly utilizing VLM features for environmental semantic understanding [9]–[11], OpenGraph employs VLMs as the frontend for multimodal cognition, segmenting object instances from visual images and converting them into textual captions. On this basis, LLMs, known for their outstanding performance in natural language processing tasks, encode these captions to enhance the semantic reasoning capabilities of maps. In addition, existing methods for constructing open-vocabulary maps often rely on depth cameras [12], which are prone to strong light interference and distance limitations. To apply to large-scale outdoor environments, OpenGraph utilizes multi-sensor calibration techniques to project caption features from 2D images onto 3D LiDAR point clouds, enabling the construction of 3D panoramic maps.

A map crucial for robotics should not only accurately represent the geometry and semantics of individual objects but also include topological relationships between objects to facilitate structured querying [13]. OpenGraph enhances the panoramic maps by constructing minimum spanning trees with instances as nodes. It incorporates geometric (position and bounding box) and semantic (caption) inputs from pairs of objects into LLMs to describe likely spatial relationships, forming an instance-layer scene graph. For expansive environments like outdoors, OpenGraph further segments the environment based on the connectivity of lane graph extracted from historical trajectories, thereby constructing a multilayer graph representation that encompasses the environment, roads, instances, lane graph, and point cloud. An example result of OpenGraph is shown in Fig. 1. The main contributions of this work are listed as follows:

- Introduction of the first outdoor open-vocabulary object-centered mapping system capable of discovering, mapping, and comprehending a vast number of instances in outdoor environments.
- Utilization of caption features as semantic representations in maps, enhancing the map’s capacity for natural language reasoning.
- Development of hierarchical graphs that facilitate rapid structured queries for specific instances within expansive environments.
- Validation on publicly outdoor dataset demonstrates that the proposed OpenGraph framework enables a profound semantic understanding of the environment and facilitates downstream applications.

The remainder of this paper proceeds as follows. Section II reviews the related works. In section III, the OpenGraph framework is introduced. Section IV shows the experimental results. Section V concludes this paper.

II. RELATED WORKS

A. Closed-vocabulary semantic mapping

While early studies [14]–[16] introduced pretrained deep learning-based segmentation models into basic spatial representations (occupancies, point clouds, etc.) for semantic 3D mapping, their performance was largely constrained by the

model capabilities. Recent researches [17], [18] exploit the latest advances in implicit neural representations to achieve geometric and semantic mapping within a unified feature space. Despite these advances, these methods require time-consuming self-supervision and are scenario-tailored, making generalization to other scenarios challenging. Most importantly, all of them either use segmentation models pretrained on a closed set of classes or can only utilize limited classes in the current scene for learning from scratch. This limitation makes them challenging to comprehend unseen object classes in complicated and open scenes.

B. Open-vocabulary 3D mapping

With the impressive progress of web-based pre-trained visual language models and large language models, an increasing number of methods are attempting to extend their 2D open vocabulary understanding capabilities to the 3D world, including the following three mainstream solutions.

1) **Vision-only point-level mapping.** Originally, OpenScene [19] achieves 3D open-vocabulary scene understanding by projecting point-wise vision features extracted from fine-tuned image segmentation model [20] onto a 3D point cloud, facilitating easy utilization for open-vocabulary queries. However, the fine-tuned models lose their original ability to capture long-tail objects. Even if subsequent works [12], [21] adopt well-designed point-wise feature extraction methods to avoid object forgetting, the inconsistency between point features blurs the boundaries of instances, making object retrieval challenging during downstream robot tasks.

2) **Vision-only instance-level mapping.** The mainstream method for instance-level open-vocabulary 3D mapping involves extracting VLM features at the 2D image mask scale and then fusing point clouds from potentially the same instances in 3D space, considering both spatial and feature similarities. Compared to OVIR-3D [22], which fuses text-aligned 2D region proposals into 3D space using Periodic 3D Instance Filtering and Merging, OpenMask3d [23] leverages predicted class-agnostic 3D instance masks to guide the multi-view fusion of CLIP-based image embeddings. Recently, Open3DIS [24] devises a 2D-guide-3D Instance Proposal Module to further enhance the description of 3D object shapes. However, the above methods still rely on fused CLIP features, which encode limited visual context under multi-view masks, thus lacking high-level natural language reasoning capabilities.

3) **Vision-language mapping.** Although not instance-level, the weakly supervised CLIP-Fields [10] first combines visual features from CLIP and textual features from Sentence-BERT [25] in the architecture of neural implicit representations as robotic semantic memory. Beyond [22], ConceptGraphs [26] further extracts structural captions for each object, feeding them to LLMs for other applications, such as LLM-powered scene graph creation and natural language reasoning. Nonetheless, their reasoning capabilities are still constrained by the utilization of underlying CLIP features, and their effectiveness in large-scale outdoor scenes is impeded by the reliance on depth cameras.

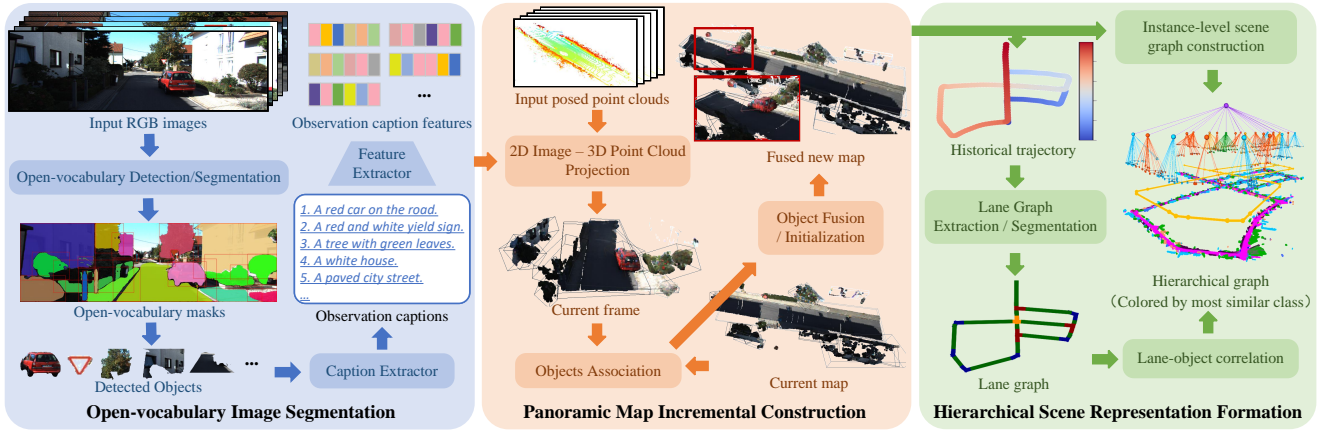


Fig. 2: The framework of OpenGraph consists of three main modules: Open-vocabulary Image Segmentation, Panoramic Map Incremental Construction, and Hierarchical Graph Representation Formation.

For OpenGraph, we employ the advanced vision language model to extract visual-textual captions directly. These captions are then encoded using LLM, yielding textual features enriched with natural language reasoning abilities.

C. 3D Scene graph

To overcome ambiguity in object retrieval by providing context-aware specifications, 3D scene graphs (3DSGs) are proposed to describe the 3D scene compactly as graph structures, where nodes represent spatial or semantic properties of objects and edges encode inter-object relationships [27]. While original approaches [28], [29] generate real-time closed-set 3D semantic scene graph predictions from image sequences using graph neural networks, recent researchers have explored integrating open-vocabulary foundation models for 3D scene graph generation. ConceptGraphs [26] and OVSG [30] pioneered an open-vocabulary framework for generating indoor robot scene graphs. However, their performance in outdoor environments is compromised by focusing solely on establishing object-level scene graphs. Inspired by closed-vocabulary 3D hierarchical graph generation methods hydra [27] and CURB-SG [13], our OpenGraph proposes the first open-vocabulary hierarchical 3D graph representation in large-scale outdoor environments.

III. OPENGRAPH

A. Framework Overview

OpenGraph takes a sequence of 2D RGB images $\mathcal{I} = \{I^{(1)}, I^{(2)}, \dots, I^{(t)}\}$ and a sequence of 3D LiDAR point clouds $\mathcal{C} = \{C^{(1)}, C^{(2)}, \dots, C^{(t)}\}$ with pose $\mathcal{P} = \{P^{(1)}, P^{(2)}, \dots, P^{(t)}\}$ as input, and produces a global hierarchical graph $\mathcal{M}_{all}^{(t)}$ of the observed environment as output (as shown in Fig. 1). The hierarchical graph consists of five layers:

- 1) **Layer 1** represents the metric-optical point cloud \mathcal{M}_{pc} , which provides the most intuitive representation of the environment.

- 2) **Layer 2** depicts the lane graph \mathcal{M}_{lg} , which possesses its topology and can be utilized for downstream tasks like path planning.
- 3) **Layer 3** is a subgraph of instances $\mathcal{M}_{ins} = \langle \mathbf{O}, \mathbf{E} \rangle$, where instances \mathbf{O} are composed of their centers of mass, bounding boxes, captions, and high-dimensional semantic features. Spatial relationships between instances are represented by edges \mathbf{E} connecting them.
- 4) **Layer 4** represents roads \mathcal{M}_{ro} , partitioned based on the connectivity of lane graph \mathcal{M}_{lg} , with each road having a center of mass.
- 5) **Layer 5** encompasses the entire outdoor environment node \mathcal{M}_{env} connected to all roads.

Edges connect nodes within each layer (e.g., to model traversability between roads) or across layers (e.g., to model that point clouds belong to an instance, or that an instance is in a certain road).

The overall OpenGraph framework, as depicted in Fig. 2, consists of three primary modules designed to operate at different dimensions of the environment representation. Firstly, the Open Vocabulary Image Segmentation module focuses on instance segmentation and feature extraction from 2D images, contributing to scene understanding at the 2D level. Secondly, the Panoramic Map Incremental Construction module is responsible for mapping 2D images and their interpretations into 3D LiDAR point clouds, enabling incremental construction of instance-layer panoramic maps. Lastly, the Hierarchical Graph Representation Formation module deals with lane graph extraction and road segmentation to construct the final hierarchical graph. By sequentially executing the three modules, OpenGraph acquires a profound understanding of the environment. The resulting hierarchical graphs and their components can be leveraged for a variety of downstream tasks.

B. Open-vocabulary Image Segmentation

Vision provides a wealth of information about the shape, size, texture, and location of objects and is an important perception for understanding the environment. The Open-

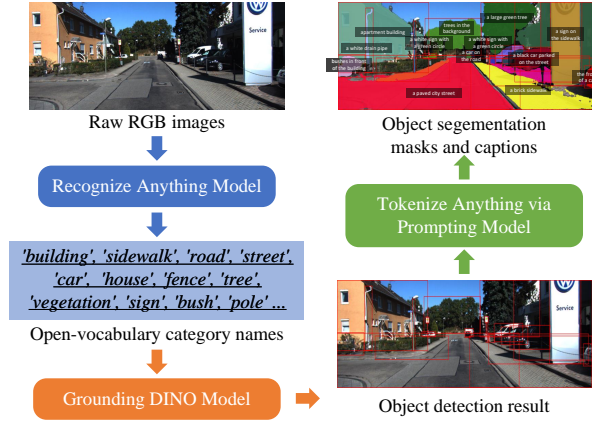


Fig. 3: We employ three sequential visual language models for image instance segmentation and caption extraction. These models sequentially perform recognition, detection, and simultaneous segmentation and description generation of objects within the input image.

vocabulary Image Segmentation module sequentially uses three visual language models to realize the caption extraction of objects in a single frame image as shown in Fig. 3.

At the current time t , for the input RGB image $I^{(t)}$, we first utilize Recognize Anything Model (RAM) [31] $\text{Rec}(\cdot)$ to recognize the categories present in it. With its open-set capability, RAM is feasible to recognize any common category, and zero-shot performance is also advantageous. Subsequently, we feed the generated open-vocabulary category names along with the original image into the Grounding DINO model [32] $\text{Det}(\cdot, \cdot)$ for open-set object detection. This yields the object detection bounding boxes, which are precisely what is required for the TAP (Tokenize Anything via Prompting) model [33] $\text{SegCap}(\cdot, \cdot)$. Prompted by the object detection bounding boxes, the TAP model segments and describes the main objects within them, producing a set of masks $\{m_i^{(t)}\}_{i=1, \dots, m}$ and a set of captions $\{c_i^{(t)}\}_{i=1, \dots, m}$ for the current frame $I^{(t)}$. The entire process can be represented as (1), and the specific model can be substituted with others possessing similar functionality.

$$\{m_i^{(t)}, c_i^{(t)}\} = \text{SegCap}\left(I^{(t)}, \text{Det}\left(I^{(t)}, \text{Seg}(I^{(t)})\right)\right) \quad (1)$$

VLMs aid in expressing the visual semantic understanding of objects through caption text, thereby facilitating the conversion from visual to language modality. However, the captions $\{c_i^{(t)}\}$ lack inherent common sense reasoning abilities. Conversely, LLMs find widespread application across various natural language processing tasks, having been pre-trained on extensive text datasets, thus boasting stronger semantic reasoning capabilities. Hence, as depicted in (2), we leverage LLMs to encode object captions, thereby generating high-dimensional embedded features to enhance comprehension and reasoning. Ensuring that features encoded in sentences of varying lengths possess uniform dimensionality facilitates subsequent retrieval based on feature similarity. Consequently, we employ the SBERT model [25] in our

experiments.

$$\mathbf{f}_i^{(t)} = \text{Embed}(c_i^{(t)}) \quad (2)$$

After processing with the foundation model described above, we derive the 2D masks $\{m_i^{(t)}\}$ and captions $\{c_i^{(t)}\}$ for candidate objects, along with their corresponding caption features $\{\mathbf{f}_i^{(t)}\}$, based on the input RGB images $I^{(t)}$ observed at the current time.

C. Panoramic Map Incremental Construction

To achieve accurate 3D mapping, it's crucial to incorporate metric information regarding detected objects. We employ a multi-sensor calibration and fusion method to project the 3D point cloud acquired from LiDAR onto a 2D image plane. Before projection, we employ 4DMOS [34] to detect and filter dynamic points from the point cloud $C^{(t)}$ to eliminate trailing shadows. The projection process generates 3D point clouds $\mathbf{p}_i^{(t)}$ of the object instances that are aligned with the corresponding masks $m_i^{(t)}$:

$$\mathbf{p}_i^{(t)} = \{l_k | K T l_k \in m_i^{(t)}, l_k \in C^{(t)}\} \quad (3)$$

where l_k is the LiDAR point, K is the internal camera parameter, and T is the external lidar-to-camera parameter. Considering the existence of bias in the calibration parameters and the noise of the sensors themselves, we use the DBSCAN clustering algorithm to reduce the noise of the point clouds $\mathbf{p}_i^{(t)}$ for each object and transform them to the map frame according to the pose $P^{(t)}$.

For objects $\mathbf{o}_i^{(t)} = \langle \mathbf{p}_i^{(t)}, c_i^{(t)}, \mathbf{f}_i^{(t)} \rangle$ detected in the current frame, we need to fuse them into the existing panoramic map $\mathbf{M}^{(t-1)} = \{\mathbf{m}_j^{(t-1)}\} = \{\langle \mathbf{p}_j^{(t-1)}, c_j^{(t-1)}, \mathbf{f}_j^{(t-1)} \rangle\}$. We compute the geometric similarity $\phi_{geo}(i, j)$, caption similarity $\phi_{cap}(i, j)$ and feature similarity $\phi_{fea}(i, j)$ of each newly detected object with all objects in the map. Geometric similarity $\phi_{geo}(i, j)$ represents the 3D bounding box Intersection over Union (IoU) of point clouds $\mathbf{p}_i^{(t)}$ and $\mathbf{p}_j^{(t-1)}$. Caption similarity $\phi_{cap}(i, j)$ is calculated using cosine similarity after vectorizing the caption text $c_i^{(t)}$ and $c_j^{(t-1)}$ with TF-IDF (Term Frequency-Inverse Document Frequency). Feature similarity $\phi_{fea}(i, j)$ is the cosine similarity between the two features $\mathbf{f}_i^{(t)}$ and $\mathbf{f}_j^{(t-1)}$. The overall similarity measure $\phi(i, j)$ is obtained as the weighted sum of the three similarities:

$$\phi(i, j) = \omega_{geo}\phi_{geo} + \omega_{cap}\phi_{cap} + \omega_{fea}\phi_{fea} \quad (4)$$

We perform object association using a greedy assignment strategy, where each newly detected object $\mathbf{o}_i^{(t)}$ is paired with the existing object $\mathbf{m}_j^{(t-1)}$ possessing the highest similarity score. If an object fails to find a match with a similarity score exceeding the threshold δ_{sim} , it is initialized as a new object in the map $\mathbf{M}^{(t)}$. For associated objects, we conduct object fusion. This involves merging the point clouds as $\mathbf{p}_j^{(t)} = \mathbf{p}_i^{(t)} \cup \mathbf{p}_j^{(t-1)}$ and updating the features as

$$\mathbf{f}_j^{(t)} = (\mathbf{f}_i^{(t)} + n_{\mathbf{m}_j} \mathbf{f}_j^{(t-1)}) / (n_{\mathbf{o}_j} + 1) \quad (5)$$

where $n_{\mathbf{m}_j}$ is the number of detections associated with \mathbf{m}_j so far. Additionally, to merge textual captions $c_i^{(t)}$ and $c_j^{(t-1)}$,

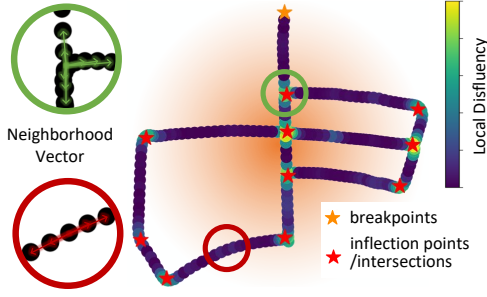


Fig. 4: We extract the lane graph \mathcal{M}_{lg} from historical trajectories $P^{(1:t)}$, whose nodes are derived from vector pinch angle $\Theta^{(n)}$ (breakpoints) and local disfluency $\lambda^{(n)}$ (inflection points or intersections).

we utilize the open-source LLM LLaMA [7] to ensure a comprehensive, conflict-free description through prompts.

After incorporating all the objects $\mathbf{o}_i^{(t)}$ of the current frame into the map, we get the incrementally updated panoramic map $\mathbf{M}^{(t)} = \{\mathbf{m}_j^{(t)}\} = \{\langle \mathbf{p}_j^{(t)}, c_j^{(t)}, \mathbf{f}_j^{(t)} \rangle\}$.

D. Hierarchical Graph Representation Formation

On the basis of the panoramic map $\mathbf{M}^{(t)}$, we generate a hierarchical graph $\mathcal{M}_{all}^{(t)}$.

For **Layer 1**, we stack the point clouds of objects as $\mathcal{M}_{pc} = \bigcup_j \mathbf{p}_j^{(t)}$ and downsample them. To enhance the visualization, we can render the point cloud using the commonly used 19 approximation categories. Specifically, we input the captions $c_j^{(t)}$ into LLaMA and prompt it to assign the most probable classes based on the content.

For **Layer 2**, lane graph \mathcal{M}_{lg} is derived from historical trajectories $P^{(1:t)}$. Initially, trajectories $P^{(1:t)}$ are projected onto a 2D plane as $\tilde{P}^{(1:t)}$ by eliminating vertical displacements. Nodes in the lane graph \mathcal{M}_{lg} represent inflection points, intersections, and breakpoints. To detect these features, we assess local disfluency $\lambda^{(n)}$ at each trajectory point $\tilde{P}^{(n)}$. Specifically, for each point, we consider a neighborhood within a radius R , forming sets of neighborhood vectors as

$$\mathbf{V}^{(n)} = \mathcal{N}(\tilde{P}^{(n)}) - \tilde{P}^{(n)} \quad (6a)$$

$$\mathcal{N}(\tilde{P}^{(n)}) = \left\{ \tilde{P}^{(m)} \mid \|\tilde{P}^{(m)} - \tilde{P}^{(n)}\| < R \right\} \quad (6b)$$

The angles are computed pairwise within the set of vectors, and the difference between each angle and 0 or π is calculated. Then, the average of the smaller values is determined and considered as the local disfluency measure:

$$\Theta^{(n)} = \left\{ \arccos \left(\frac{v_i \cdot v_j}{\|v_i\| \cdot \|v_j\|} \right) \right\}, \forall v_i, v_j \in \mathbf{V}^{(n)} \quad (7a)$$

$$\lambda^{(n)} = \text{mean}(\min(|\theta_i|, |\theta_i - \pi|)), \forall \theta_i \in \Theta^{(n)} \quad (7b)$$

We employed DBSCAN to cluster trajectory points exhibiting disfluency exceeding a threshold δ_{dis} , thereby identifying inflection points and intersections. To discern breakpoints, we assess whether the mean of $\Theta^{(n)}$ is proximate to 0. Fig. 4 exemplifies the detection of lane graph nodes. The edges of the lane graph \mathcal{M}_{lg} are subsequently derived

from the inter-node links and are trimmed based on trajectory alignment.

For **Layer 3**, we calculate the bounding box and center of mass for each object $\mathbf{m}_j^{(t)}$ within the panoramic map $\mathbf{M}^{(t)}$, treating them as nodes \mathbf{O} . Subsequently, we compute the bounding box IoUs between pairs of objects, resulting in a dense graph which we refine by estimating a Minimum Spanning Tree (MST). Additionally, to infer relations among nodes, we feed the captions, poses and bounding boxes of object pairs into LLaMA, yielding an open-vocabulary instance-layer scene graph $\mathcal{M}_{ins} = \langle \mathbf{O}, \mathbf{E} \rangle$. The nodes \mathbf{O} are connected to the corresponding point cloud in Layer 1.

For **Layer 4**, connectivity within lane graph \mathcal{M}_{lg} forms the foundation for distinguishing roads as \mathcal{M}_{ro} . We designate a small section of the path as a subordinate area near inflection and intersection points on the lane graph. Additionally, intersections have been further categorized into "intersections" and "T-intersections". Inflection points are defined as "L-intersections". The stretch of roadway that doesn't intersect with any inflection or intersection points is termed the "straight roadway". The nodes \mathbf{O} in Layer 3 are linked to the closest road segment.

For **Layer 5**, we construct a global environment node \mathcal{M}_{env} that connects all road segments \mathcal{M}_{ro} in Layer 4.

Collectively, the aforementioned layers constitute a comprehensive OpenGraph $\mathcal{M}_{all}^{(t)}$ that encompasses a semantic comprehension and a hierarchical topology of the scenario.

IV. EXPERIMENTAL RESULTS

In this section, the performance of the proposed OpenGraph is validated through experiments performed on the public outdoor dataset SemanticKITTI [38].

A. 3D Semantic Segmentation

As discussed in subsection III-D, we leverage LLaMA for point cloud segmentation at Layer 1 based on SemanticKITTI's provided 19 classes. For a comparison of 3D segmentation results, we selected three classes of methods as baselines. The first class is a point cloud segmentation method directly trained and fine-tuned on the SemanticKITTI dataset, RangeNet++ [35]. We generate a global semantic map using its predicted labels. The second class comprises 2D image segmentation methods trained on outdoor image datasets, including DeepLab v3 [36] and DecoupleSegNets [37]. We derive 3D semantic maps by projecting their image segmentation onto point clouds. The third class involves the direct utilization of VLM features to replace caption features in OpenGraph, specifically CLIP [3] and BLIP [5]. Here, each object is assigned a class based on the textual features closest to its visual features.

We selected three sequences from SemanticKITTI: short (03), medium (05), and long (08). As shown in Fig. 5, due to point-level segmentation in 2D or 3D, the fully supervised approaches generate many scattered points. Additionally, small objects like bicycles suffer from lower segmentation accuracy due to limited training samples. While CLIP and BLIP, two methods employing VLM features for scene

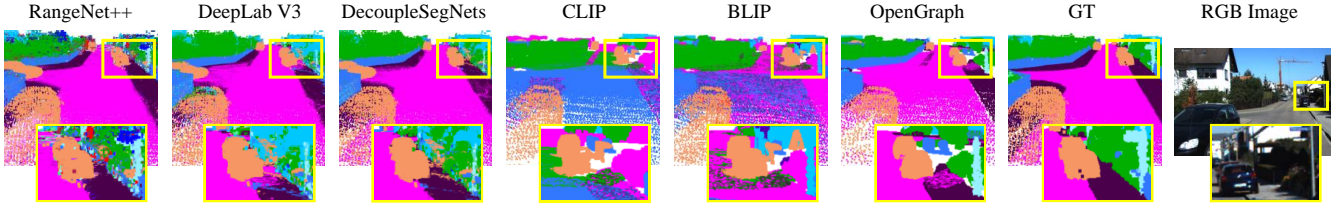


Fig. 5: Semantic segmentation results on the SemanticKITTI dataset, utilizing 19 classes, indicate that despite not undergoing fine-tuning, OpenGraph demonstrates higher segmentation accuracy and reduced noise levels.

TABLE I: Quantitative Results (IoU and F1 Score) of Semantic Segmentation on SemanticKITTI Dataset

Seq.	Method	Car	Road	Sidewalk	Building	Fence	Veget.	Pole	T-sign	Average	F1 Score
03	RangeNet++ [35]	0.4191	0.8096	0.4656	0.3962	0.3483	0.5410	0.1245	0.1302	0.4780	0.6115
	DeepLab V3 [36]	0.2535	0.6784	0.3392	0.3262	0.0632	0.5445	0.1270	0.1521	0.4626	0.6025
	DecoupleSegNets [37]	0.3075	0.8283	0.5314	0.3912	0.0646	0.6624	0.1412	0.2457	0.6025	0.7277
	CLIP [3]	0.5851	0.4349	0.0000	0.1654	0.0823	0.3497	0.0000	0.0138	0.3972	0.5797
	BLIP [5]	0.3215	0.4478	0.0000	0.3240	0.0227	0.3789	0.0122	0.1202	0.4017	0.5673
	OpenGraph	0.4191	0.7299	0.2552	0.1737	0.6599	0.0083	0.2960	0.0000	0.6051	0.7302
05	RangeNet++ [35]	0.5634	0.8575	0.5591	0.5933	0.3605	0.5368	0.1285	0.0950	0.4990	0.6200
	DeepLab V3 [36]	0.3627	0.7731	0.3749	0.5094	0.2855	0.6066	0.0986	0.0388	0.5203	0.6579
	DecoupleSegNets [37]	0.4489	0.8501	0.5850	0.5228	0.3022	0.6293	0.1260	0.0845	0.5895	0.7212
	CLIP [3]	0.5618	0.0356	0.0000	0.1769	0.3427	0.0028	0.0312	0.0000	0.2964	0.4518
	BLIP [5]	0.5997	0.4334	0.0000	0.3318	0.1237	0.1926	0.0000	0.0342	0.3320	0.4781
	OpenGraph	0.7000	0.7963	0.4823	0.7961	0.3957	0.6312	0.1552	0.1056	0.6598	0.7749
08	RangeNet++ [35]	0.6339	0.8214	0.4786	0.5500	0.1086	0.6083	0.1607	0.1504	0.5111	0.6295
	DeepLab V3 [36]	0.4167	0.7162	0.3087	0.4923	0.0736	0.6758	0.1074	0.0691	0.5425	0.6733
	DecoupleSegNets [37]	0.4445	0.8370	0.4870	0.5414	0.0845	0.7152	0.1026	0.0631	0.6376	0.7576
	CLIP [3]	0.3942	0.3456	0.0000	0.2439	0.0952	0.2166	0.0033	0.0693	0.2753	0.4130
	BLIP [5]	0.4025	0.4318	0.0000	0.3909	0.0633	0.2840	0.0008	0.0422	0.3677	0.5250
	OpenGraph	0.6667	0.7436	0.3594	0.7581	0.1447	0.6384	0.1892	0.1635	0.6463	0.7633

TABLE II: Quantitative Results (top-1,2,3 recall) of Object Retrieval

Seq.	Query-Type	Methods	R@1	R@2	R@3	#Query
03/05/08	Ontology	CLIP [3]	0.60	0.70	0.73	30
		BLIP [5]	0.50	0.60	0.70	
		OpenGraph	0.90	0.90	0.90	
		OpenGraph-LLM	0.70	0.80	0.87	
	Proximity	CLIP [3]	0.37	0.47	0.53	30
		BLIP [5]	0.30	0.40	0.47	
		OpenGraph	0.80	0.87	0.87	
		OpenGraph-LLM	0.70	0.73	0.80	
	Functionality	CLIP [3]	0.47	0.53	0.57	30
		BLIP [5]	0.37	0.37	0.47	
		OpenGraph	0.63	0.80	0.80	
		OpenGraph-LLM	0.67	0.80	0.87	

understanding, fail to achieve accurate object classification, OpenGraph excels in this aspect with the assistance of LLM features. Tab. I presents the results of semantic segmentation quantification, including IoU for common classes and overall F1 scores. Notably, OpenGraph outperforms even comparable fully supervised methods across these sequences.

B. Open-vocabulary Object Retrieval

To illustrate the advantages of OpenGraph for open-vocabulary complex semantic queries, we conducted object retrieval experiments that center around three distinct text types:

Ontology: A direct description of the object itself. For instance, *A tall tree*.

Proximity: The description of the object relies on objects related to it. For example, *I want to find some green leaves* (a tree or a bush).

Functionality: The description focuses on the inferred functions of the object in question. For instance, *Something that can be used for driving* (a car).

The experiments involve small segments extracted from the three sequences, each containing a diverse array of objects. For each query type on each sequence, we generated 10 distinct descriptions, with relevant objects manually chosen as ground truth values. The Fig. 6 illustrates some of the comparison results of OpenGraph with other zero-shot methods, where the colors are rendered according to the degree of similarity of the features (VLM features for CLIP and BLIP, LLM features for OpenGraph). Since OpenGraph maintains an explicit caption for each object, it facilitates effortless access to LLM for object retrieval, denoted as *OpenGraph-LLM*. To elaborate, we feed both the map object captions and query text into GPT [6], tasking it with identifying the top three most pertinent objects, labeled red, green, and blue, respectively. Tab. II presents the overall top-1, top-2, and top-3 recall measurements.

First, in ontology queries, OpenGraph demonstrates the highest recall rate, mitigating the positional bias when LLM is applied, such as recognizing a toilet in a previously observed RV. Secondly, in proximity queries, the performance of VLM-based methods sharply drops, due to limited natural language comprehension like 'symbol of light' versus

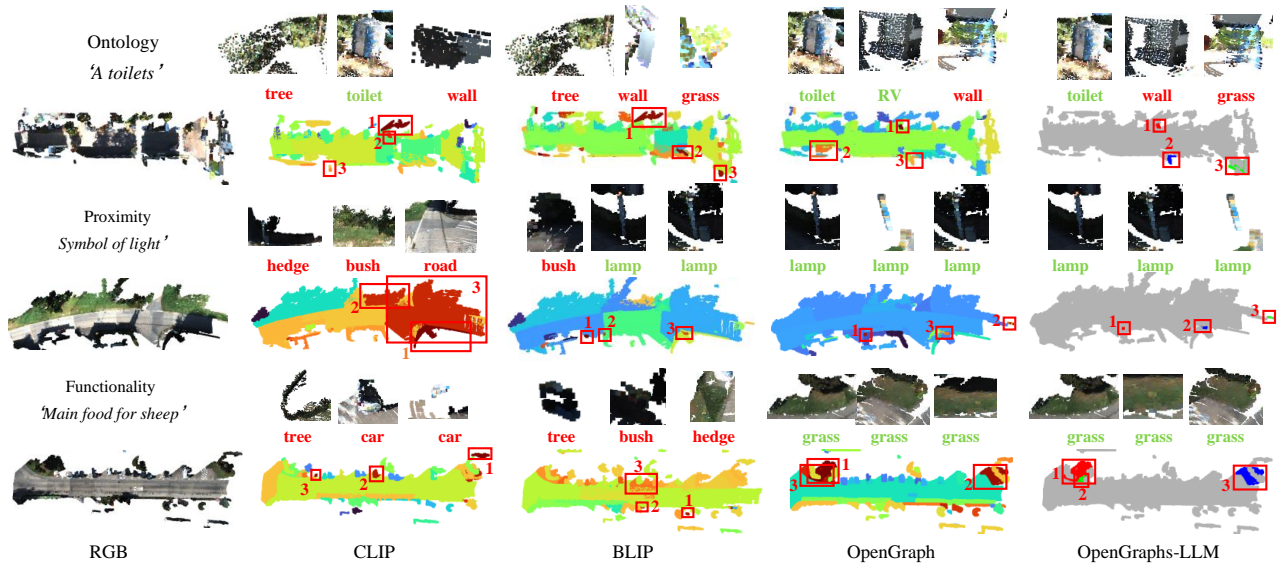


Fig. 6: The outcomes from various open-vocabulary text queries (displaying the Top-3 objects). In the visual representation, OpenGraph-LLM highlights the Top-3 objects in red, green, and blue, while the other methods render all objects based on relevance. The text beneath each retrieved object in the figure corresponds to its actual category, where green signifies successful retrieval and red indicates failure.

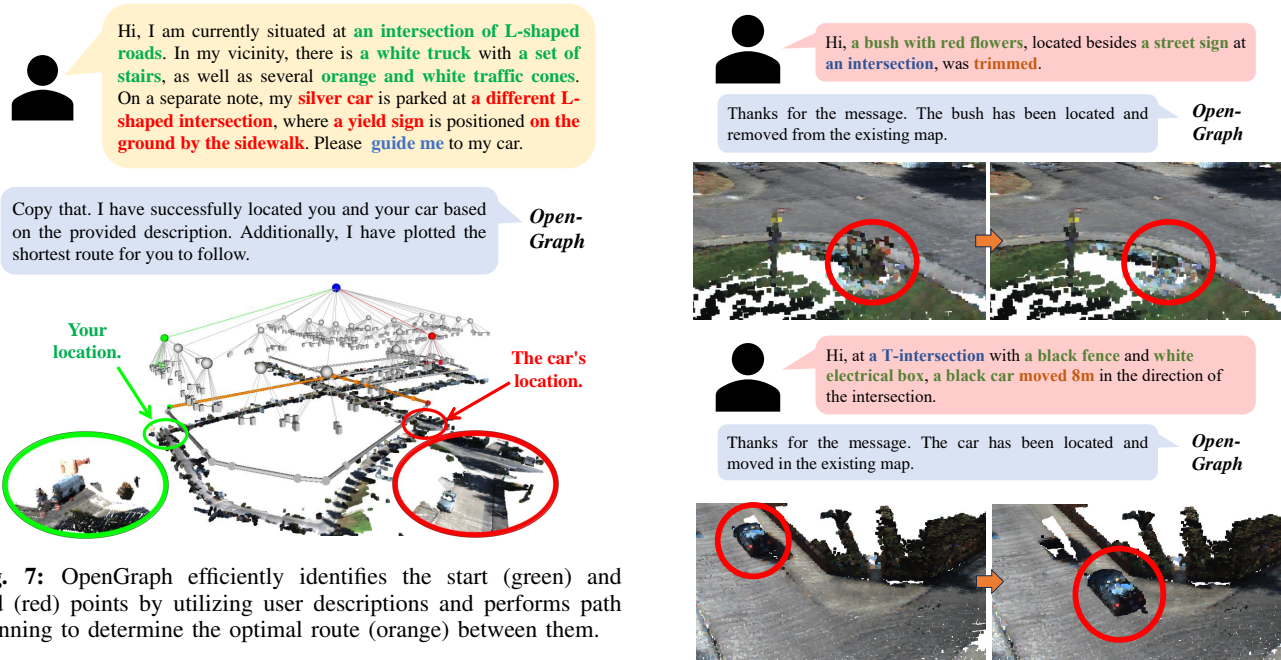


Fig. 7: OpenGraph efficiently identifies the start (green) and end (red) points by utilizing user descriptions and performs path planning to determine the optimal route (orange) between them.

'lamp'. Lastly, OpenGraph excels in challenging functional queries with LLM boosting its natural language reasoning. In summary, OpenGraph and its LLM variants demonstrate superior natural language reasoning in a variety of outdoor object retrieval tasks.

C. Hierarchical Graph Structured Query

Hierarchical graphs offer the benefit of structured top-down queries. By integrating with LLMs on the front end, OpenGraph empowers users to accomplish a wide range of tasks more effectively and efficiently. Imagine the queriers situated within a scene, capable of observing only a limited

Fig. 8: OpenGraph relies on user-supplied map patches to update the map. Here shows the updated point cloud in Layer 1.

portion of their surroundings. By indicating the type of road (Layer 4) they are on and the relationships between objects nearby ((Layer 3), they can swiftly localize themselves. Moreover, if they can provide hints about their destination, OpenGraph can facilitate global path planning on the lane graph to guide them effectively. A related case is shown in Fig. 7.

Furthermore, OpenGraph facilitates human-interactive map updates. Individuals within the environment can con-

tribute the latest map patches to OpenGraph by detecting changes in their surroundings, ensuring the continual upkeep of the environment map. Fig. 8 visually demonstrates this process, where a person actively observes the removal of a bush beneath a street sign at an intersection. OpenGraph promptly identifies the object based on the description and promptly updates the map accordingly.

V. CONCLUSION

This paper introduces OpenGraph, an open vocabulary hierarchical 3D graph representation framework for large-scale outdoor environments. Initially, the extraction of instance masks, captions, and features occurs at the 2D image level, facilitated by VLMs and LLMs. Subsequently, a panoramic map is incrementally constructed and fused by projecting onto a 3D point cloud. Finally, the extraction of lane maps and subsequent scene segmentation culminates in the derivation of a hierarchical graph. The results from evaluations on public real datasets reveal that OpenGraph, operating as a zero-shot method, even exhibits superior performance in 3D semantic segmentation compared to fully supervised methods, while also demonstrating advantages in open vocabulary querying over alternative types. Moreover, the framework facilitates rapid structured queries.

Moving forward, our future endeavors entail the integration of OpenGraph with more advanced VLMs and LLMs. This integration aims to imbue the edges between instances with richer semantic and provide component-level understanding.

REFERENCES

- [1] A. Hornung, *et al.*, “Octomap: An efficient probabilistic 3d mapping framework based on octrees,” *Autonomous robots*, vol. 34, no. 3, pp. 189–206, 2013.
- [2] Y. Deng, *et al.*, “See-csom: Sharp-edged and efficient continuous semantic occupancy mapping for mobile robots,” *IEEE Transactions on Industrial Electronics*, 2023.
- [3] A. Radford, *et al.*, “Learning transferable visual models from natural language supervision,” in *International conference on machine learning*, pp. 8748–8763. PMLR, 2021.
- [4] C. Jia, *et al.*, “Scaling up visual and vision-language representation learning with noisy text supervision,” in *International conference on machine learning*, pp. 4904–4916. PMLR, 2021.
- [5] J. Li, *et al.*, “Blip: Bootstrapping language-image pre-training for unified vision-language understanding and generation,” in *International Conference on Machine Learning*, pp. 12 888–12 900. PMLR, 2022.
- [6] J. Achiam, *et al.*, “Gpt-4 technical report,” *arXiv preprint arXiv:2303.08774*, 2023.
- [7] H. Touvron, *et al.*, “Llama: Open and efficient foundation language models,” *arXiv preprint arXiv:2302.13971*, 2023.
- [8] A. Chowdhery, *et al.*, “Palm: Scaling language modeling with pathways,” *Journal of Machine Learning Research*, vol. 24, no. 240, pp. 1–113, 2023.
- [9] C. Huang, *et al.*, “Visual language maps for robot navigation,” in *2023 IEEE International Conference on Robotics and Automation (ICRA)*, pp. 10 608–10 615. IEEE, 2023.
- [10] N. M. M. Shafiullah, *et al.*, “Clip-fields: Weakly supervised semantic fields for robotic memory,” *arXiv preprint arXiv:2210.05663*, 2022.
- [11] K. Blomqvist, *et al.*, “Neural implicit vision-language feature fields,” *arXiv preprint arXiv:2303.10962*, 2023.
- [12] K. M. Jatavallabhula, *et al.*, “Conceptfusion: Open-set multimodal 3d mapping,” *arXiv preprint arXiv:2302.07241*, 2023.
- [13] E. Greve, *et al.*, “Collaborative dynamic 3d scene graphs for automated driving,” *arXiv preprint arXiv:2309.06635*, 2023.
- [14] S. Yang, *et al.*, “Semantic 3d occupancy mapping through efficient high order crfs,” in *2017 IEEE/RSJ International Conference on Intelligent Robots and Systems (IROS)*, pp. 590–597. IEEE, 2017.
- [15] Y. Deng, *et al.*, “S-mki: Incremental dense semantic occupancy reconstruction through multi-entropy kernel inference,” in *2022 IEEE/RSJ International Conference on Intelligent Robots and Systems (IROS)*, pp. 3824–3829. IEEE, 2022.
- [16] Y. Deng, *et al.*, “Hd-ccsom: Hierarchical and dense collaborative continuous semantic occupancy mapping through label diffusion,” in *2022 IEEE/RSJ International Conference on Intelligent Robots and Systems (IROS)*, pp. 2417–2422. IEEE, 2022.
- [17] Y. Haghighi, *et al.*, “Neural implicit dense semantic slam,” *arXiv preprint arXiv:2304.14560*, 2023.
- [18] Y. Shi, *et al.*, “City-scale continual neural semantic mapping with three-layer sampling and panoptic representation,” *Knowledge-Based Systems*, vol. 284, p. 111145, 2024.
- [19] S. Peng, *et al.*, “Openscene: 3d scene understanding with open vocabularies,” in *Proceedings of the IEEE/CVF Conference on Computer Vision and Pattern Recognition*, pp. 815–824, 2023.
- [20] B. Li, *et al.*, “Language-driven semantic segmentation,” *CoRR*, vol. abs/2201.03546, 2022. [Online]. Available: <https://arxiv.org/abs/2201.03546>
- [21] J. Kerr, *et al.*, “Lerf: Language embedded radiance fields,” in *Proceedings of the IEEE/CVF International Conference on Computer Vision*, pp. 19 729–19 739, 2023.
- [22] S. Lu, *et al.*, “Ovir-3d: Open-vocabulary 3d instance retrieval without training on 3d data,” in *Conference on Robot Learning*, pp. 1610–1620. PMLR, 2023.
- [23] A. Takmaz, *et al.*, “Openmask3d: Open-vocabulary 3d instance segmentation,” *arXiv preprint arXiv:2306.13631*, 2023.
- [24] P. D. Nguyen, *et al.*, “Open3dis: Open-vocabulary 3d instance segmentation with 2d mask guidance,” *arXiv preprint arXiv:2312.10671*, 2023.
- [25] N. Reimers, *et al.*, “Sentence-bert: Sentence embeddings using siamese bert-networks,” *arXiv preprint arXiv:1908.10084*, 2019.
- [26] Q. Gu, *et al.*, “Conceptgraphs: Open-vocabulary 3d scene graphs for perception and planning,” *arXiv preprint arXiv:2309.16650*, 2023.
- [27] N. Hughes, *et al.*, “Hydra: A real-time spatial perception system for 3d scene graph construction and optimization,” *arXiv preprint arXiv:2201.13360*, 2022.
- [28] S.-C. Wu, *et al.*, “Scenegrphfusion: Incremental 3d scene graph prediction from rgb-d sequences,” in *Proceedings of the IEEE/CVF Conference on Computer Vision and Pattern Recognition*, pp. 7515–7525, 2021.
- [29] S.-C. Wu, *et al.*, “Incremental 3d semantic scene graph prediction from rgb sequences,” in *Proceedings of the IEEE/CVF Conference on Computer Vision and Pattern Recognition*, pp. 5064–5074, 2023.
- [30] H. Chang, *et al.*, “Context-aware entity grounding with open-vocabulary 3d scene graphs,” *arXiv preprint arXiv:2309.15940*, 2023.
- [31] Y. Zhang, *et al.*, “Recognize anything: A strong image tagging model,” *arXiv preprint arXiv:2306.03514*, 2023.
- [32] S. Liu, *et al.*, “Grounding dino: Marrying dino with grounded pre-training for open-set object detection,” *arXiv preprint arXiv:2303.05499*, 2023.
- [33] T. Pan, *et al.*, “Tokenize anything via prompting,” *arXiv preprint arXiv:2312.09128*, 2023.
- [34] B. Mersch, *et al.*, “Receding Moving Object Segmentation in 3D LiDAR Data Using Sparse 4D Convolutions,” *IEEE Robotics and Automation Letters (RA-L)*, vol. 7, no. 3, pp. 7503–7510, 2022.
- [35] A. Milioto, *et al.*, “Rangenet++: Fast and accurate lidar semantic segmentation,” in *2019 IEEE/RSJ International Conference on Intelligent Robots and Systems (IROS)*, pp. 4213–4220. IEEE, 2019.
- [36] L.-C. Chen, *et al.*, “Encoder-decoder with atrous separable convolution for semantic image segmentation,” in *Proceedings of the European conference on computer vision (ECCV)*, pp. 801–818, 2018.
- [37] X. Li, *et al.*, “Improving semantic segmentation via decoupled body and edge supervision,” in *Computer Vision–ECCV 2020: 16th European Conference, Glasgow, UK, August 23–28, 2020, Proceedings, Part XVII 16*, pp. 435–452. Springer, 2020.
- [38] J. Behley, *et al.*, “Towards 3D LiDAR-based semantic scene understanding of 3D point cloud sequences: The SemanticKITTI Dataset,” *The International Journal on Robotics Research*, vol. 40, DOI 10.1177/02783649211006735, no. 8-9, pp. 959–967, 2021.